IEEE Access
Multidisciplinary ⋮ Rapid Review ⋮ Open Access Journal

Received July 18, 2020, accepted July 25, 2020, date of publication July 28, 2020, date of current version August 6, 2020.

Digital Object Identifier 10.1109/ACCESS.2020.3012545

Frequency-Diverse Metasurface Antenna With Hybrid Bunching Methods for Coincidence Imaging

MENGRAN ZHAO[1], **(Graduate Student Member, IEEE), SHITAO ZHU**[1,2], **HUILIN HUANG**[1],
XIAOMING CHEN[1], **(Senior Member, IEEE), JUAN CHEN**[1], **(Member, IEEE),**
AND ANXUE ZHANG[1]
[1]Key Laboratory of Multifunctional Materials and Structures, School of Information and Communication Engineering,
Ministry of Education, Xi'an Jiaotong University, Xi'an 710049, China
[2]National Lab of Radar Signal Processing, Xidian University, Xi'an 710071, China

Corresponding authors: Shitao Zhu (shitaozhu@xjtu.edu.cn) and Juan Chen (chen.juan.0201@xjtu.edu.cn)

This work was supported in part by the Natural Science Foundation of Shaanxi Province under Grant 2017ZDXM-GY-009and Grant 2020JM-078; in part by the China Postdoctoral Science Foundation under Grant 2017M613136; in part by the Shaanxi Province Postdoctoral Science Foundation under Grant 2017BSHYDZZ13; and in part by the Fundamental Research Funds for the Central Universities under Grant xzy022019068.

ABSTRACT A frequency-diverse metasurface antenna with hybrid bunching methods for coincidence imaging is proposed in this paper. The hybrid frequency-diverse bunching metasurface antenna contains an excitation system, a frequency-diverse metasurface and a double-layer-metal-plate bunching system. Firstly, the excitation system of the metasurface antenna is divided into two parts, the bunching-excitation module and the random-excitation module. The bunching-excitation module includes a seven-element coherent antenna array that can generate bunching beams with 80 degree beamwidth from 32GHz to 36GHz; and the random-excitation module includes eight antenna elements distributed evenly to excite the frequency-diverse metasurface in the same working bandwidth. A multilayer feed system is also designed utilizing the stripline structure to feed both the bunching-excitation module and the random-excitation module. Secondly, six kinds of metamaterial elements possessing disparate transmitted phases are selected to constitute the frequency-diverse metasurface. The frequency-diverse metasurface is loaded to the excitation system to generate the frequency-diverse radiation patterns. Then, in order to achieve a narrower bunching angle, a double-layer-metal-plate bunching system is designed. Furthermore, the performances of the proposed bunching metasurface antenna, including the radiation efficiency, the reflection coefficient and the correlation coefficients of radiation patterns at different frequencies are evaluated. Finally, the coincidence imaging experiment is carried out using the proposed hybrid bunching metasurface antenna and the image of the target is reconstructed successfully. The designed is verified by both simulations and measurements.

INDEX TERMS Metasurface, frequency-diverse, hybrid bunching methods, coincidence imaging.

I. INTRODUCTION

High accuracy and fast imaging system of microwave and millimeter wave has been widely used in security check, precision guidance and medical imaging. However, the existing imaging system such as the synthetic aperture radar (SAR) imaging system and the phased array radar (PAR) imaging system have difficulties in balancing low system complexity, high imaging accuracy and fast imaging speed. The adoption of metamaterial offers a new method. Metamaterials are artificial structures that have been widely used in many fields, such as perfect lens [1], electromagnetic cloak [2] and several kinds of metasurface antennas [3]–[10]. The frequency-diverse metasurface antenna is a new kind of metamaterial based aperture antenna that can generate different radiation patterns at different frequencies. Each radiation pattern can be used as a measurement mode in the application of coincidence imaging.

In 2013, a metaimager was first proposed by J. Hunt and colleagues. They also fabricated a prototype to demonstrate

The associate editor coordinating the review of this manuscript and approving it for publication was Abhishek K. Jha.

the feasibility of microwave holographic imaging [11]–[13]. In 2014, J. Hunt demonstrated a microwave imaging system that combines computational imaging techniques with metamaterial aperture antenna design [14]. This work was the pioneering research of the metamaterial antenna based multisensor fusion computational imaging system. From 2015 to 2018, T. Sleasman presented a series of dynamic metamaterial aperture antennas designed for schemes of microwave computational imaging [15]–[20]. The dynamic metamaterial aperture antenna was composed of metamaterial elements with diodes connected to an external control circuit. The combination of diodes and passive metamaterial elements brought forward a new idea in designing metamaterial. In 2016, J. Bai proposed a new method of millimeter wave compressive sensing imaging by combining the patch antenna and the coded frequency-selective surface (FSS) [21]. The element of coded FSS loaded with PIN diodes can be switched to ''off'' to transmit the incident wave or ''on'' to reflect the incident wave. Different radiation patterns can be acquired at a single frequency by switching the sate of each PIN diode randomly. In 2017, T. Sleasman investigated the use of a dynamic metasurface as the transmitting antenna for a SAR imaging system [22]. The combination of traditional imaging system and metamaterial-based imaging system provided a new way for the application of metamaterial aperture. In 2018, M. F. Imani proposed a single-port two-dimensional dynamic metasurface aperture capable of generating a multitude of distinct illumination patterns at microwave frequencies [23]. The cavity-backed design and the possibility of single frequency computational imaging has profound significance. In 2019, A. Molaei proposed a compressive reflector antenna with surface specially tailored by digitized metamaterial absorbers [24]. The metamaterial reflector antenna based millimeter-wave imaging system is a new form of computational imaging system that has promising development.

However, the radiation patterns generated by the antennas mentioned above usually cover theta from −90° to 90°. The beams out of the target region would worsen the imaging conditions. To solve this problem, the concept of bunching random beam is proposed by M. Zhao in 2018 [25]. The bunching random beam can concentrate the energy on the target region while containing the low correlation feature of radiation patterns at different center frequencies. In 2019, M. Zhao proposed a bunching metasurface antenna utilizing a broadband patch antenna array and a frequency-diverse quasi-gradient metalens [26]. This is a transmission metasurface antenna utilizing the gradient zoom coefficient design to generate frequency-diverse bunching radiation patterns. In 2020, O. Yurduseven proposed a lens-loaded coded aperture that can increase information capacity [27]. It is a cavity metasurface antenna with a semi-spherical shaped dielectric lens that can focus the beams on the target and improve the number of effective measurement modes.

In order to generate frequency-diverse bunching random (FDBR) radiation patterns, a hybrid method is proposed in this paper. Ref. [25] used the ''waved metal plate'' to bunch the totally non-orientation random radiation patterns and the bunching angle is above 100°. Ref. [26] utilized the ''gradient zoom coefficient design'' to bunch random radiation patterns with a certain bunching angle and the final bunching angle is around 90°. The bunching method used in this work is to superpose the random radiation patterns generated by the random excitation module (REM) onto the bunching radiation patterns generated by the bunching excitation module (BEM), which is different from previous works in principle. The bunching angle of this work is 60°, which is narrower than that of Ref. [25] (100°) and Ref. [26] (90°). The FDBR radiation patterns can be divided into two parts, the bunching radiation patterns and the frequency-diverse random radiation patterns. In the Section II, a excitation system is firstly proposed, which contains the BEM and the REM. Besides, a multilayer feed module (MFM) utilizing the stripline structure is designed to feed both the BEM and the REM. In the Section III, six kinds of metamaterial elements possessing disparate transmitted phases are chosen to constitute the frequency-diverse metasurface. In the Section IV, a double-layer-metal-plate (DLMP) bunching system is proposed, which provides a narrower bunching angle as well as mechanical support. In the Section V, the performances of the proposed hybrid frequency-diverse bunching metasurface antenna (HFDBMA), including the radiation efficiency, the reflection coefficient and the correlation coefficients of radiation patterns at different frequencies are evaluated. The design is validated by both simulated and measured results. In the Section VI, a coincidence imaging experiment using the HFDBMA is implemented, and image of the target is reconstructed with high quality.

II. THE EXCITATION SYSTEM

The FDBR radiation patterns generated by the HFDBMA is divided into two parts, the bunching radiation patterns and the frequency-diverse random radiation patterns. Thus, the antenna array is designed to be two-part, the BEM and the REM, respectively. To feed both the BEM and the REM, a MFM is also designed utilizing the metallic-via based stripline structure. The BEM, the REM and the MFM together constitute the excitation system of the HFDBMA.

A. DESIGN OF THE BEM AND THE REM

The BEM is shown in Fig. 1(a), which includes a seven-element coherent antenna array that can generate bunching beams with 60° beamwidth from 32GHz to 36GHz as shown in Fig. 1(b). The BEM is designed to generate bunching beams with narrow main lobe and low side lobes. High side lobes of the BEM would excite the metasurface and influence the effect of bunching beam. The antenna unit is firstly designed as shown in Fig. 1(a), which is a patch antenna with a stem and two slots to ensure the wide working bandwidth. As shown in Fig. 1(c), the reflection coefficient of the antenna unit is under −16dB from 32GHz to 36GHz, which guarantees the feed efficiency.

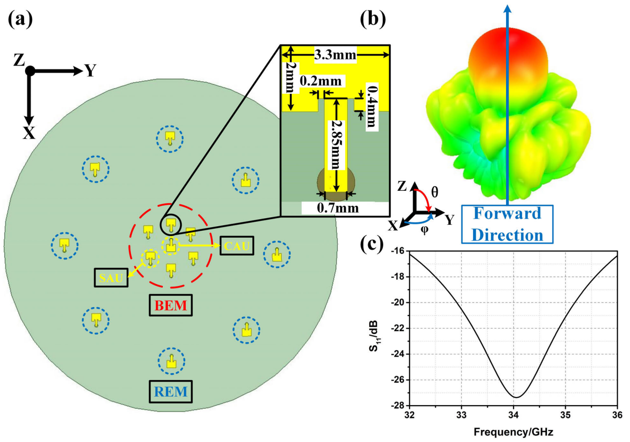

FIGURE 1. (a) The BEM, the REM and the antenna unit; (b) Bunching beam with 80 degree beamwidth; (c) The reflection coefficient of the antenna unit.

The thickness of the substrate is 1.58mm and the permittivity of the REM and the BEM is 2.55. The BEM is composed of seven antenna units, one central antenna unit (CAU) and six surrounding antenna units (SAUs). The feeding power of the CAU is twice as large as that of the SAUs and the feeding phase difference of the CAU and the SAUs is 180° due to the inversion of the CAU. The CAU is inverse to meet the requirement of the feed system which will be explained in Chapter 2.2. According to the theory of circular antenna array, the seven-element antenna array can achieve narrow main lobe while containing low side lobes. As shown in Fig. 1(a), the REM is composed of eight antenna units that are distributed evenly over the aperture to excite the frequency-diverse metasurface. The radius of the BEM and the REM is 7mm and 30mm, respectively.

B. DESIGN OF THE MFM

According to the design of the BEM and the REM, totally 15 antenna units are used. Thus, a feed system (i.e., MFM) is designed according to the requirements of both the BEM and the REM. The thickness of the substrate is 1.58mm and the permittivity of the MFM is 2.55. The diameter of the MFM is 110mm. The MFM is composed of a double-layer 1-7 divider feeding the BEM and a double-layer 1-8 divider feeding the REM. In this Chapter, a single-layer 1-2 divider is firstly designed as the foundation unit of the MFM. Then, a double-layer 1-4 divider is designed to validate the feasibility of multilayer design method. Finally, the 1-7 divider and the 1-8 divider is designed following the multilayer design method. Furthermore, the MFM is connected with the BEM and the REM, which constitutes the excitation system.

In order the transmit energy efficiently from the feed port to the antenna within the working bandwidth, a broadband power divider is designed utilizing the metallic-via based stripline structure. A single-layer 1-2 divider is firstly designed as shown in Fig. 2(a). The top metal layer is removed in Fig. 2(a) to show that the stripline structure that is sandwiched in the substrate. The performance of the divider including the reflection coefficient S_{11} and the transmission coefficient S_{21} is shown in Fig. 2(b). From Fig. 2(b), the S_{11} is under −17dB and the S_{21} is around −3.25dB from 32GHz to 36GHz, which promise good performance of the 1-2 divider.

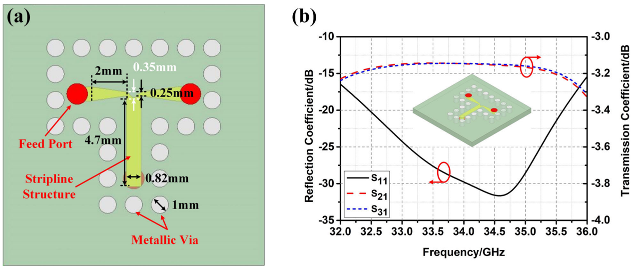

FIGURE 2. (a) The structure of the metallic-via based single-layer 1-2 divider; (b) The reflection coefficient S_{11} and the transmission coefficient S_{21} of the designed 1-2 divider.

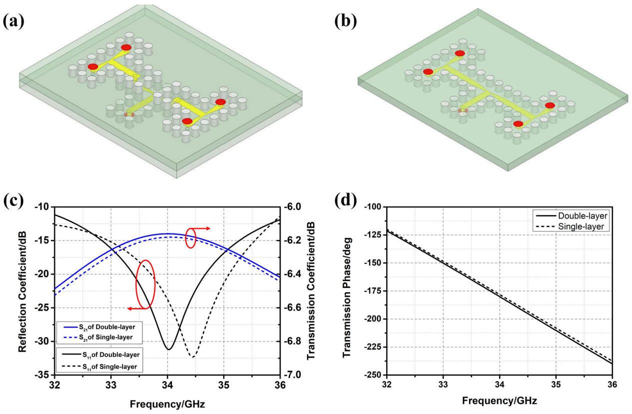

FIGURE 3. (a) The structure of the double-layer 1-4 divider; (b) The structure of the single-layer 1-4 divider; (c) Comparison of the reflection coefficients S_{11} and the transmission coefficients S_{21} of two dividers; (d) Comparison of the transmission phases of two dividers.

Then, a double-layer 1-4 divider is designed by piling three single-layer 1-2 dividers as shown in Fig. 3(a). To validate the feasibility of the multilayer design method, a single-layer 1-4 divider is designed by cascading three single-layer 1-2 dividers as shown in Fig. 3(b). The performance comparison of two 1-4 dividers are shown in Fig. 3(c) and Fig. 3(d), from which can draw the conclusion that multilayer design is feasible and can achieve good performance as single-layer design. The top layer of the double-layer 1-4 divider can rotate freely while maintaining the same performance, which means the multilayer design method can save space and minimize the size of divider. This feature is suitable to feed compact antenna arrays.

According to the analysis in Chapter 2.1, a 1-7 divider with one branch has twice power is designed following the multilayer design method. As shown in Fig. 4(a), a double-layer 1-7 divider is designed by piling one 1-4 single-layer divider and three 1-2 single-layer dividers. In order to connect the 1-7 divider and the BEM, the layout of branches should be designed preciously. However, it's impossible to connect the

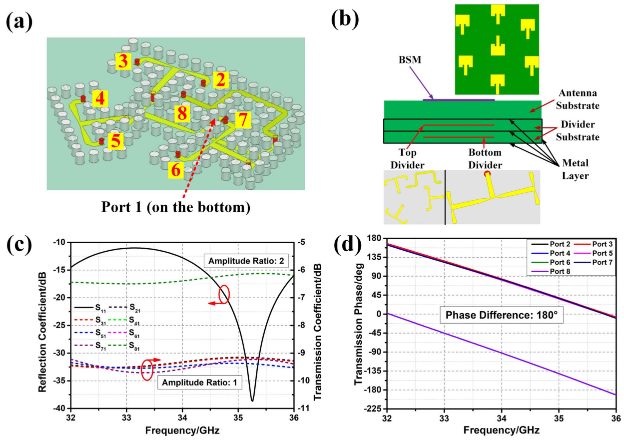

FIGURE 4. **(a) The structure of the double-layer 1-7 divider; (b) Connection of the 1-7 divider and the BEM; (c) The reflection coefficient and the transmission coefficients of different branches; (d) The realization of 180° phase difference.**

1-7 divider and the BEM when antenna units have the same orientation. So the CAU of the BEM is inverse to make the connection feasible as shown in Fig. 4(b). The performance of the 1-7 divider is shown in Fig. 4(c). The transmission coefficients of six branches are around −9.5dB and that of the branch with twice power is around −6.25dB. The transmission phases of the 1-7 divider is shown in Fig. 4(d), which have a 180° phase difference as designed in Chapter 2.1. The design of the 1-8 divider feeding the REM is following the same method.

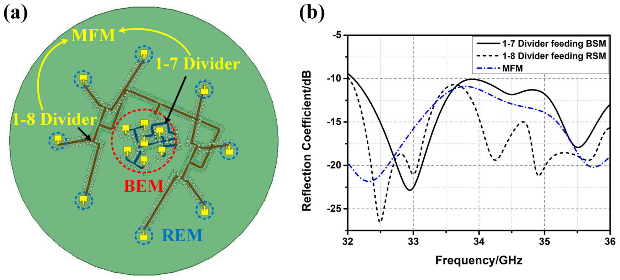

FIGURE 5. **(a) The schematic of the excitation system; (b) The reflection coefficients of the 1-7 divider feeding the BEM, the 1-8 divider feeding the REM and the MFM.**

As shown in Fig. 5(a), the MFM, the BEM and the REM together comprise the excitation system. The MFM consists of the 1-7 divider feeding the BEM and the 1-8 divider feeding the REM. The reflection coefficients of the 1-7 divider connecting the BEM, the 1-8 divider connecting the REM and the MFM connecting the 15 antenna units (i.e., including both the BEM and the REM) are shown in Fig. 5(b), respectively. From Fig. 5(b), the reflection coefficient of the excitation system (i.e., the reflection coefficient of the MFM) is under −10dB from 32GHz to 36GHz, which promises the feed efficiency.

III. THE FREQUENCY-DIVERSE METASURFACE

The complementary electric inductive-capacitive (cELC) element is used to analyze how the metasurface can generate frequency-diverse radiation patterns according to the previous work of G. Lipworth presented in 2015 [28] and D. R. Smith presented in 2017 [29].

As radiating elements, cELCs have been shown to exhibit a magnetic dipole response when excited by magnetic field [13,14]. So the cELCs can be regarded as magnetic polarizable dipoles $\vec{m}_i$ with expression shown as equation (1)

$$\vec{m}_i = \alpha_{m,i}(\omega)\vec{H}(x_i) \tag{1}$$

where $\vec{H}(x_i)$ is the magnetic field at the location x_i and $\alpha_{m,i}(\omega)$ is a polarizability described by the Lorentzian form (2)

$$\alpha_{m,i}(\omega) = \frac{F\omega^2}{\omega_0^2 - \omega^2 + j\Gamma\omega} \tag{2}$$

where F is the oscillator factor, ω_0 is the resonance frequency and Γ is the damping factor. $\omega_0 = \sqrt{LC}$ relates to the inductance and capacitance of the equivalent resonant circuit of the metamaterial element, and can be tuned by modifying the local permittivity, modifying the geometry and structure of the metamaterial element, or by integrating lumped passive or active elements [29].

The electric field illuminating the target plane can be computed through superposition of the fields radiated from all dipoles. According to [28], the electric field at location $\vec{r}$ in the target can be expressed as equation (3)

$$\vec{E}(\vec{r}) = j\frac{\omega\mu}{4\pi}\sum_n (\vec{m}_n \times \hat{r})(\frac{jk}{R_n} - \frac{1}{R_n^2})e^{jkR_n} \tag{3}$$

According to the analysis above and the Babinet principle [30]–[32], the metamaterial elements can be regarded as electric dipoles. When the dipoles are distributed at random positions and excited with random amplitudes and different initial phases, the electric field that illuminating the target plane would be random. Therefore, the metasurface consisting of different metamaterial elements with different transmission amplitudes and phases that distributed at random positions would generate random radiation patterns when excited by the REM. Since the transmission amplitudes and phases of metamaterial elements are different from frequency to frequency, the radiation patterns generated by the metasurface are also frequency-diverse.

Following the same design idea in [26], six metamaterial elements are selected to form the metasurface as shown in Fig. 6(a). The thickness of the substrate is 0.508mm and the permittivity of the metasurface is 2.65. The diameter of the frequency-diverse metasurface is 110mm. When excited by the REM, the metasurface can generate random radiation patterns that are superposed onto the bunching beam as shown in Fig. 6(b), which is suitable to be used as measurement modes in coincidence imaging.

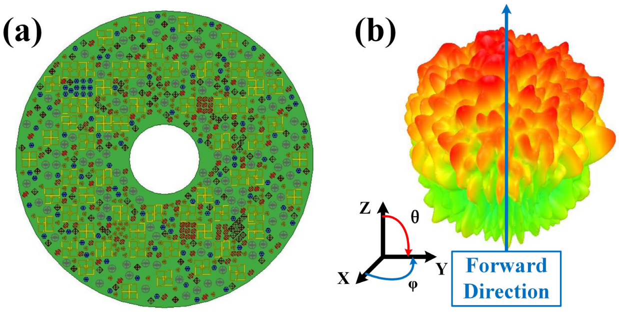

FIGURE 6. **(a) The designed metasurface using the selected metamaterial elements; (b) The random radiation patterns generated by the metasurface.**

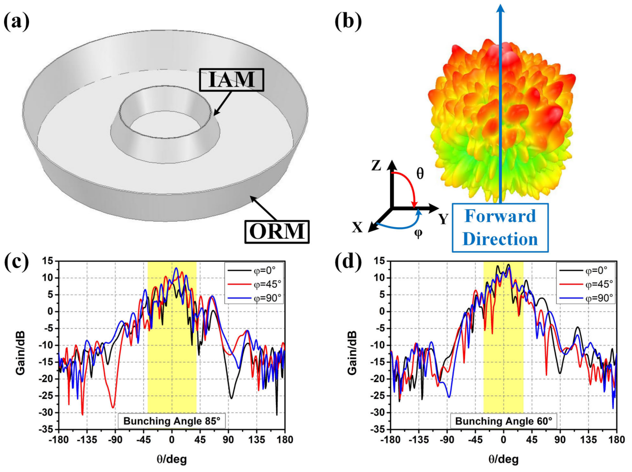

FIGURE 7. **(a) The DLMP bunching system; (b) Typical bunching random radiation patterns; (c) Radiation pattern without the DLMP; (d) Radiation pattern with the DLMP.**

IV. THE DLMP BUNCHING SYSTEM

The FDBR radiation patterns is generated by a hybrid method. As designed above, the random radiation patterns is preliminarily bunched by superposing the frequency-diverse random beams to the bunching beam. However, the bunching angle of this method is only 85°. In order to reduce the bunching angle, a DLMP bunching system is designed as shown in Fig. 7(a), which reduces the bunching angle to 60° as well as provides mechanical support.

The DLMP is composed of two parts, the inner anti-interference module (AIM) and the outer random-bunching module (ORM). The AIM contains a taper ring with a dip angle of 18°, which is used to protect the BEM from being interfered by the REM. The ORM consists a metal ring with a dip angle of 20°, which is used to bunch the non-orientated frequency-diverse random radiation patterns. The diameter of the AIM and the ORM is 16mm and 110mm, respectively. The height of the AIM is 20mm and that of the ORM is 30mm. A typical bunching random radiation patterns generated by the HFDBMA are shown in Fig. 7(b). The bunching angle of the radiation pattern without the DLMP is 85° as shown in Fig. 7(c) and that of the radiation pattern with the DLMP is 60° as shown in Fig. 7(d), which illustrates the effectiveness of the application of the DLMP.

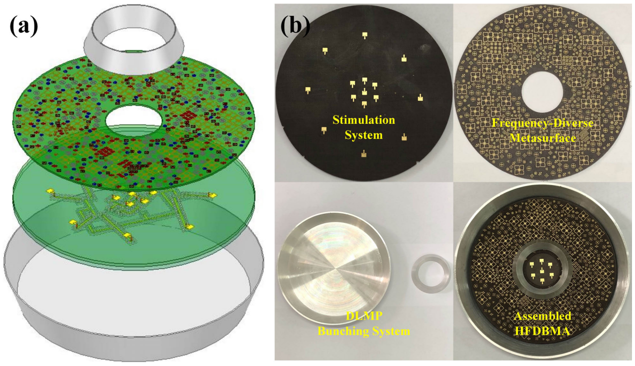

FIGURE 8. **(a) The schematic of the HFDBMA; (b) The fabricated excitation system, frequency-diverse metasurface, DLMP bunching system and the assembled HFDBMA.**

V. SIMULATED AND MEASURED RESULTS

To validate the design of the HFDBMA, a prototype is fabricated as shown in Fig. 8. The substrate of the excitation system is TACONIC TLX-8 (permittivity 2.55), and the substrate of the frequency-diverse metasurface is TACONIC TLX-6 (permittivity 2.65). The schematic of the HFDBMA is shown in Fig. 8(a). The components of the HFDBMA and the assembled HFDBMA are shown in Fig. 8(b). All the components of the HFDBMA are fit together using the hot-melt adhesive. The diameter of the HFDBMA is 110mm.

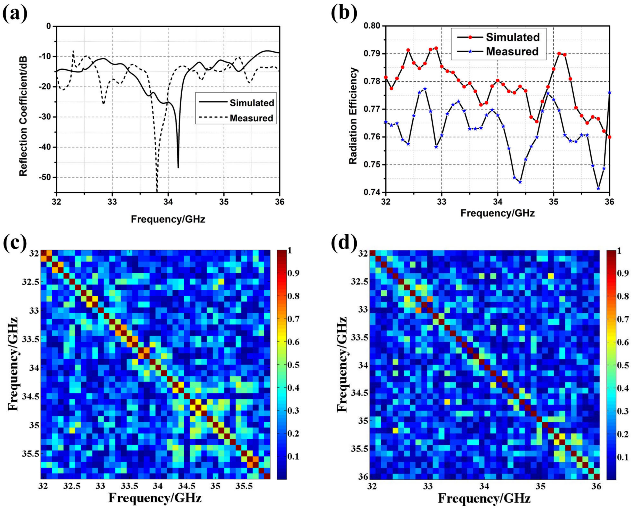

FIGURE 9. **Comparison of simulated and measured (a) reflection coefficient S_{11}; (b)radiation efficiency; (c), (d) correlation coefficients of radiation patterns at different frequencies.**

Fig. 9 shows the simulated and measured results of the proposed HFDBMA. As shown in Fig. 9(a), the HFDBMA is well-fed since both the simulated and measured reflection coefficients S_{11} of the HFDBMA are under −10dB from 32GHz to 36GHz. The S_{11} is measured using the vector network analyzer (VNA) E8363B of Agilent. The measuring system is calibrated using the kit 85052D of Agilent and the Short-Open-Load-Thru (SOLT) method. The radiation efficiency of the HFDBMA is shown in Fig. 9(b). The average measured radiation efficiency is around 0.76 within the working bandwidth, which is a little lower than that of the simulated. The radiation patterns of the HFDBMA are designed to serve as measurement modes in coincidence imaging, which requires that different measurement modes should be low-correlated [33], [34]. As shown in Fig. 9(c) and Fig. 9(d), the correlation coefficients of both measured and simulated radiation patterns at different frequencies are evaluated. The amplitudes and the phases of different radiation patterns are arranged to complex matrices, which are used to calculate the cross-correlation (i.e., the correlation coefficients of different radiation patterns). The normalized correlation coefficients of measurement modes at frequencies shown on the x-axis and the y-axis, which are represented by the pixels shown in Fig. 9(c) and Fig. 9(d). The majority correlation coefficients of the simulated measurement modes are under 0.42 as shown in Fig. 9(c). Because of the error from fabrication, assembling and the measurement, most correlation coefficients of the measured measurement modes are under 0.35 as shown in Fig. 9(d), which are lower than those of the simulated. The good performance of the HFDBMA in coincidence imaging is guaranteed by both simulated and measured results [33].

VI. COINCIDENCE IMAGING EXPERIMENT

The measurement modes (i.e., diverse radiation patterns) are needed in coincidence imaging. The measurement modes should be independent to each other in ideal situation. According to the measurements, the majority correlation coefficients of radiation patterns generated by the HFDBMA are under 0.35. Thus, the measurement equation matrix can be formed utilizing all the measured data [35]:

$$
\begin{aligned}
S_t &= S_R\sigma + n \\
S_t &= \begin{bmatrix} S_t(t_1) \\ S_t(t_1) \\ \vdots \\ S_t(t_M) \end{bmatrix}, \quad \sigma = \begin{bmatrix} \sigma(I_1) \\ \sigma(I_2) \\ \vdots \\ \sigma(I_Q) \end{bmatrix}, \; n = \begin{bmatrix} n(t_1) \\ n(t_2) \\ \vdots \\ n(t_M) \end{bmatrix}, \\
S_R &= \begin{bmatrix} S_R(I_1, t_1) & S_R(I_2, t_1) & \cdots & S_R(I_Q, t_1) \\ S_R(I_1, t_2) & S_R(I_2, t_2) & \cdots & S_R(I_Q, t_2) \\ \vdots & \vdots & & \vdots \\ S_R(I_Q, t_M) & S_R(I_Q, t_M) & \cdots & S_R(I_Q, t_M) \end{bmatrix},
\end{aligned} \tag{4}
$$

where $S_t(t_m)$ is the measured data, $S_R(I_q, t_m)$ is the measurement mode distribution in the imaging plane, I_q represents the discrete imaging point, $\sigma(I_q)$ is the scatterring coefficient at the $I_q th$ imaging point, t_m represents the index of the measurements, $n(t_m)$ is the noise. The equation (4) can be solved using fast iterative shrinkage threshold algorithm (FISTA) method [36] or the conjugate gradient least squares algorithm (CGLSA) [37] with high efficiency. Thus, the high quality image can be reconstructed using all the measured data of the HFDBMA.

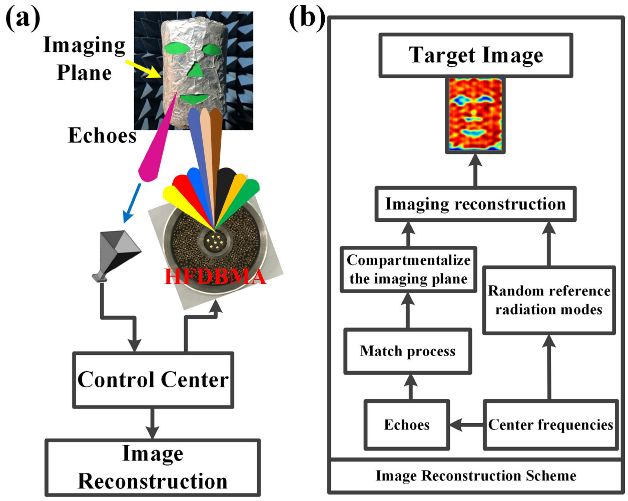

FIGURE 10. (a) The schematic of the coincidence imaging; (b) The flowchart of the coincidence imaging.

The schematic of the coincidence imaging is shown in Fig. 10(a). The transmitting antenna is the HFDBMA to emit FDBR radiation patterns and the receiving antenna is a horn antenna to obtain the echo data. The target is within the 3dB beamwidth of FDBR radiation patterns. The diameter of the HFDBMA is 110mm and the imaging distance between the target and the HFDBMA is 100cm. The coincidence imaging flowchart is shown in Fig. 10(b). The match process contains two parts (i.e., the match between the measurement modes and the echoes and the target distance estimation).

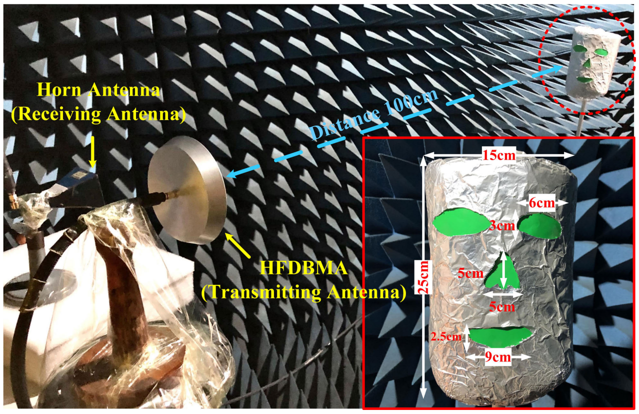

FIGURE 11. Coincidence imaging experiments.

The scene of the experiment of coincidence imaging is shown in Fig. 11. A model of human face is placed at the imaging plane as the target. As shown in the bottom right corner of Fig. 11, the model of human face is 15cm × 25cm. The face is covered with tinfoil expect the green part, which is hollowed out as the eyes, the nose and the mouth.

The dimensions are marked as shown in the figure. The imaging plane contains $K_1 \times K_2$ imaging cells and is equally discretized, where K_1 is in the azimuth direction and K_2 is in the pitch direction. The side length of the imaging cell is $1cm$ (about 1/5 of the 3dB beamwidth of the coherent transmitting aperture with the same size of the HFDBMA) in both directions. The quality of the image is evaluated by the index entropy. The entropy of an image is defined as [38]

$$E = \sum_{x=1}^{X}\sum_{y=1}^{Y} D(x, y)\ln[D(x, y)] \tag{5}$$

where $D(x, y) = |d(x, y)|/\sum_{x=1}^{X}\sum_{y=1}^{Y}|d(x, y)|$, $d(x, y)$ is the data of image in the imaging plane, and $X \times Y$ is the imaging area.

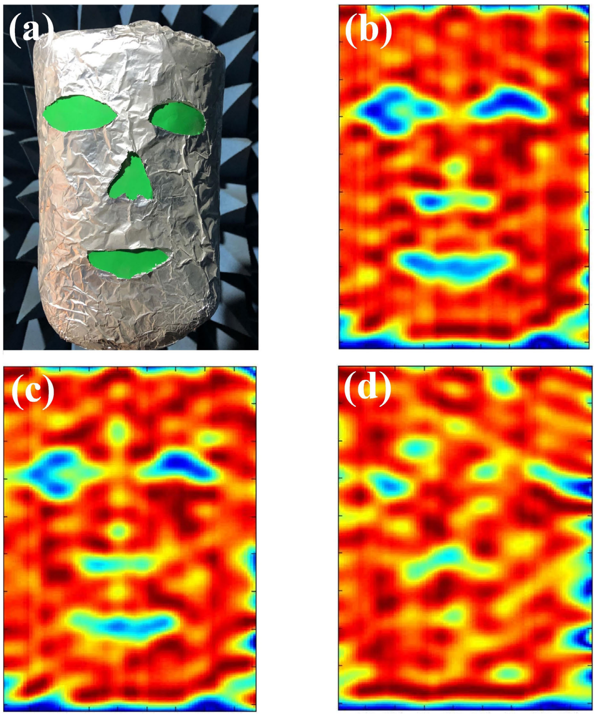

FIGURE 12. **(a) The origin image; The reconstructed image when the SNR is (b) 15dB; (c) 11dB; (d) 8dB.**

As shown in Fig. 12, the image of the human face is reconstructed using the HFDBMA. Subject to the experimental condition, the highest SNR is 18dB. The origin image is shown in Fig. 12(a) and the reconstructed image with high quality is shown in Fig. 12(b) when the SNR is higher than 15dB. The quality of the reconstructed image declines with the decreases of the SNR. As shown in Fig. 12(c), the reconstructed human face can be distinguished when the SNR is 11dB. When the SNR is lower than 8dB, the reconstructed face is completely drown in background noise as shown in Fig. 12(d). Through thirty independent experiments, the average entropies of the reconstructed image shown in the Fig. 12(b), Fig. 12(c) and Fig. 12(d) are 9.18, 9.43 and 10.01, respectively.

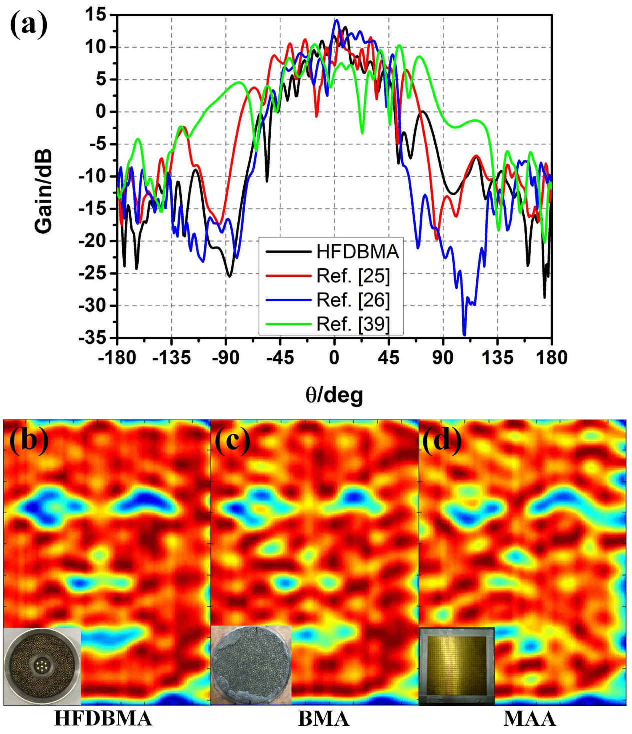

FIGURE 13. **(a) Comparison of radiations of previous works and the proposed HFDBMA; The reconstructed image using (b) the HFDBMA; (c) the BMA and (d) the MAA.**

In order to illustrate the advantage of the bunching feature, a bunching metasurface antenna (BMA) proposed in [26] and a metamaterial aperture antenna (MAA) without bunching feature proposed in [39] is used for comparison. The side length of the MAA is 120mm, which is almost the same with the diameter of the HFDBMA (110mm) and the BMA. Fig. 13(a) shows the comparison of radiation patterns of previous works in [25], [26], [39] and the proposed HFDBMA. The method proposed in this manuscript can generate narrower bunching angle than previous works, which promises better imaging result when the SNR is bad. However, the cost and the system complexity of the HFDBMA is much higher than previous designs. Fig. 13(b)-(d) show the comparison of the reconstructed images using the HFDBMA, the BMA and the MAA under the same experiment condition. The human face image reconstructed by the HFDBMA and the BMA (i.e., Fig. 13(b)(c)) can be seen clearly while that reconstructed by the MAA can hardly be recognized (i.e., Fig. 13(d)). Through thirty independent experiments, the average entropies of the reconstructed images shown in Fig. 13(b),Fig. 13(c) and Fig. 13(d) are 9.18, 9.65 and 9.82. The comparison experiment demonstrates the metasurface antenna with bunching feature can reconstruct image with higher quality than that without bunching feature, which illustrates the advantages of the bunching feature. What's more, the image reconstructed by the HFDBMA is better than that reconstructed by the BMA under the same experiment condition. The entropy of the image reconstructed by the HFDBMA is lower than that of the image reconstructed by the BMA. The coincidence imaging results illustrate the superiority of the hybrid bunching method.

VII. CONCLUSION

In this paper, a frequency-diverse metasurface antenna with hybrid bunching methods for coincidence imaging has been proposed. The hybrid frequency-diverse bunching metasurface antenna (HFDBMA) is composed of the excitation system, the frequency-diverse metasurface and the double-layer-metal-plate (DLMP) bunching system. The excitation system contains the bunching-excitation module (BEM), the random-excitation module (REM) and the multilayer feed module (MFM). The DLMP bunching system includes the inner anti-interference module (AIM) and the outer random-bunching module (ORM). Firstly, the BEM consists of one central antenna unit (CAU) and six surrounding antenna units (SAUs) has been designed that can generate bunching beams with 80 degree beamwidth from 32GHz to 36GHz. Furthermore, a 1-7 power divider with one branch (i.e., the one that connects the CAU) has twice power has been designed following the multilayer design to feed the BEM. The REM and the 1-8 power divider feeding the REM have also been designed according to the same method. Then, based on the analysis of the metamaterial element and previous researches, six metamaterial elements have been selected to form the frequency-diverse metasurface. Besides, a double-layer-metal-plate (DLMP) bunching system has been designed to achieve a narrower bunching angle as well as to provide mechanical support. Finally, the coincidence imaging experiment using the HFDBMA has been implemented and the image of the target has been reconstructed. The performance of the HFDBMA have been verified through simulations and measurements.

REFERENCES

[1] J. B. Pendry, "Negative refraction makes a perfect lens," *Phys. Rev. Lett.*, vol. 85, no. 18, pp. 3966–3969, Oct. 2000.

[2] D. Schurig, J. J. Mock, B. J. Justice, S. A. Cummer, J. B. Pendry, A. F. Starr, and D. R. Smith, "Metamaterial electromagnetic cloak at microwave frequencies," *Science*, vol. 314, no. 5801, pp. 977–980, Nov. 2006.

[3] H. Shi, L. Wang, M. Zhao, J. Chen, A. Zhang, and Z. Xu, "Transparent metasurface for generating microwave vortex beams with cross-polarization conversion," *Materials*, vol. 11, no. 12, p. 2448, Dec. 2018.

[4] H. Shi, L. Wang, G. Peng, X. Chen, J. Li, S. Zhu, A. Zhang, and Z. Xu, "Generation of multiple modes microwave vortex beams using active metasurface," *IEEE Antennas Wireless Propag. Lett.*, vol. 18, no. 1, pp. 59–63, Jan. 2019.

[5] A. P. Feresidis, G. Goussetis, S. Wang, and J. C. Vardaxoglou, "Artificial magnetic conductor surfaces and their application to low-profile high-gain planar antennas," *IEEE Trans. Antennas Propag.*, vol. 53, no. 1, pp. 209–215, Jan. 2005.

[6] H. Zhou, Z. Pei, S. Qu, S. Zhang, J. Wang, Z. Duan, H. Ma, and Z. Xu, "A novel high-directivity microstrip patch antenna based on zero-index metamaterial," *IEEE Antennas Wireless Propag. Lett.*, vol. 8, pp. 538–541, 2009.

[7] F. Qureshi, M. A. Antoniades, and G. V. Eleftheriades, "A compact and low-profile metamaterial ring antenna with vertical polarization," *IEEE Antennas Wireless Propag. Lett.*, vol. 4, pp. 333–336, 2005.

[8] M. Rahman, D.-S. Ko, and J.-D. Park, "A compact multiple notched ultra-wide band antenna with an analysis of the CSRR-TO-CSRR coupling for portable UWB applications," *Sensors*, vol. 17, no. 10, p. 2174, Sep. 2017.

[9] F. J. Herraiz-Martinez, V. Gonzalez-Posadas, L. E. Garcia-Munoz, and D. Segovia-Vargas, "Multifrequency and dual-mode patch antennas partially filled with left-handed structures," *IEEE Trans. Antennas Propag.*, vol. 56, no. 8, pp. 2527–2539, Aug. 2008.

[10] Q. Hou, H. Tang, Y. Liu, and X. Zhao, "Dual-frequency and broadband circular patch antennas with a monopole-type pattern based on epsilon-negative transmission line," *IEEE Antennas Wireless Propag. Lett.*, vol. 11, pp. 442–445, 2012.

[11] J. Hunt, T. Driscoll, A. Mrozack, G. Lipworth, M. Reynolds, D. Brady, and D. R. Smith, "Metamaterial apertures for computational imaging," *Science*, vol. 339, no. 6117, pp. 310–313, Jan. 2013.

[12] G. Lipworth, A. Mrozack, J. Hunt, D. L. Marks, T. Driscoll, D. Brady, and D. R. Smith, "Metamaterial apertures for coherent computational imaging on the physical layer," *J. Opt. Soc. Amer. A, Opt. Image Sci.*, vol. 30, pp. 1603–1612, Aug. 2013.

[13] G. Lipworth, J. Hunt, A. Mrozack, D. Brady, and D. R. Smith, "Simulations of 2D metamaterial apertures for coherent computational imaging," in *Proc. IEEE Int. Conf. Microw., Commun., Antennas Electron. Syst. (COMCAS)*, Tel Aviv, Israel, Oct. 2013, pp. 1–4.

[14] J. Hunt, J. Gollub, T. Driscoll, G. Lipworth, A. Mrozack, M. S. Reynolds, D. J. Brady, and D. R. Smith, "Metamaterial microwave holographic imaging system," *J. Opt. Soc. Amer. A, Opt. Image Sci.*, vol. 31, pp. 2109–2119, Oct. 2014.

[15] T. Sleasman, M. F. Imani, J. N. Gollub, and D. R. Smith, "Dynamic metamaterial aperture for microwave imaging," *Appl. Phys. Lett.*, vol. 107, no. 20, Nov. 2015, Art. no. 204104.

[16] T. Sleasman, M. F. Imani, J. N. Gollub, and D. R. Smith, "Microwave imaging using a disordered cavity with a dynamically tunable impedance surface," *Phys. Rev. A, Gen. Phys.*, vol. 6, no. 5, Nov. 2016, Art. no. 054019.

[17] M. Boyarsky, T. Sleasman, L. Pulido-Mancera, A. V. Diebold, M. F. Imani, and D. R. Smith, "Single-frequency 3D synthetic aperture imaging with dynamic metasurface antennas," *Appl. Opt.*, vol. 57, pp. 4123–4134, May 2018.

[18] A. V. Diebold, M. F. Imani, T. Sleasman, and D. R. Smith, "Phaseless computational ghost imaging at microwave frequencies using a dynamic metasurface aperture," *Appl. Opt.*, vol. 57, no. 9, pp. 2142–2149, Mar. 2018.

[19] A. Pedross-Engel, C. M. Watts, D. R. Smith, and M. S. Reynolds, "Enhanced resolution stripmap mode using dynamic metasurface antennas," *IEEE Trans. Geosci. Remote Sens.*, vol. 55, no. 7, pp. 3764–3772, Jul. 2017.

[20] O. Yurduseven, D. L. Marks, T. Fromenteze, and D. R. Smith, "Dynamically reconfigurable holographic metasurface aperture for a Mills-Cross monochromatic microwave camera," *Opt. Express.*, vol. 26, pp. 5281–5291, Mar. 2018.

[21] J.-J. Bai, W.-B. Chen, Z.-H. Deng, G.-F. Zhang, and Y.-Q. Fu, "Millimetre wave compressive sensing imaging based on coded frequency selective surface," *J. Electromagn. Waves Appl.*, vol. 30, no. 9, pp. 1171–1182, Jun. 2016.

[22] T. Fromenteze, O. Yurduseven, M. F. Imani, J. Gollub, C. Decroze, D. Carsenat, and D. R. Smith, "Computational imaging using a mode-mixing cavity at microwave frequencies," *Appl. Phys. Lett.*, vol. 106, no. 19, May 2015, Art. no. 194104.

[23] M. F. Imani, T. Sleasman, and D. R. Smith, "Two-dimensional dynamic metasurface apertures for computational microwave imaging," *IEEE Antennas Wireless Propag. Lett.*, vol. 17, no. 12, pp. 2299–2303, Dec. 2018.

[24] A. Molaei, J. Heredia-Juesas, G. Ghazi, J. Vlahakis, and J. A. Martinez-Lorenzo, "Digitized metamaterial absorber-based compressive reflector antenna for high sensing capacity imaging," *IEEE Access*, vol. 7, pp. 1160–1173, 2019.

[25] M. Zhao, S. Zhu, X. Chen, J. Li, D. Hu, L. Wang, and A. Zhang, "Frequency-diverse transmission metamaterial aperture with a bunching random beam," *IEEE Antennas Wireless Propag. Lett.*, vol. 17, no. 6, pp. 1029–1033, Jun. 2018.

[26] M. Zhao, S. Zhu, J. Li, H. Shi, J. Chen, Y. He, and A. Zhang, "Frequency-diverse bunching metamaterial antenna for coincidence imaging," *Materials*, vol. 12, no. 11, p. 1817, Jun. 2019.

[27] O. Yurduseven, M. A. B. Abbasi, T. Fromenteze, and V. Fusco, "Lens-loaded coded aperture with increased information capacity for computational microwave imaging," *Remote Sens.*, vol. 12, no. 9, p. 1531, May 2020.

[28] G. Lipworth, A. Rose, O. Yurduseven, V. R. Gowda, M. F. Imani, H. Odabasi, P. Trofatter, J. Gollub, and D. R. Smith, "Comprehensive simulation platform for a metamaterial imaging system," *Appl. Opt.*, vol. 54, pp. 9343–9353, Nov. 2015.

[29] D. R. Smith, O. Yurduseven, L. P. Mancera, P. Bowen, and N. B. Kundtz, "Analysis of a waveguide-fed metasurface antenna," *Phys. Rev. A, Gen. Phys.*, vol. 8, no. 5, Nov. 2017, Art. no. 054048.

[30] X. Liu, W. Li, Z. Zhao, R. Lu, S. Zhu, Z. Xu, X. Chen, and A. Zhang, "Babinet principle for anisotropic metasurface with different substrates under obliquely incident plane wave," *IEEE Trans. Microw. Theory Techn.*, vol. 66, no. 6, pp. 2704–2713, Jun. 2018.

[31] X. Liu, R. Lu, S. Zhu, Z. Xu, X. Chen, and A. Zhang, "Analysis of complementary metasurfaces based on the babinet principle," *IEEE Microw. Wireless Compon. Lett.*, vol. 29, no. 1, pp. 8–10, Jan. 2019.

[32] X. Liu, J. Zhang, X. Chen, Z. H. Jiang, and A. Zhang, "A generalized accurate model for complementary periodic subwavelength metasurface based on babinet principle," *IEEE Trans. Antennas Propag.*, vol. 68, no. 5, pp. 3780–3790, May 2020.

[33] S. Zhu, M. Zhao, X. Dong, H. Shi, R. Lu, X. Chen, and A. Zhang, "Differential coincidence imaging with frequency diverse aperture," *IEEE Antennas Wireless Propag. Lett.*, vol. 17, no. 6, pp. 964–968, Jun. 2018.

[34] S. Zhu, X. Dong, Y. He, M. Zhao, G. Dong, X. Chen, and A. Zhang, "Frequency-polarization-diverse aperture for coincidence imaging," *IEEE Microw. Wireless Compon. Lett.*, vol. 28, no. 1, pp. 82–84, Jan. 2018.

[35] S. Zhu, Y. He, H. Shi, A. Zhang, Z. Xu, and X. Dong, "Mixed mode radar coincidence imaging with hybrid excitation radar array," *IEEE Trans. Aerosp. Electron. Syst.*, vol. 54, no. 4, pp. 1589–1604, Aug. 2018.

[36] M. Z. A. Bhotto, M. O. Ahmad, and M. N. S. Swamy, "An improved fast iterative shrinkage thresholding algorithm for image deblurring," *SIAM J. Imag. Sci.*, vol. 8, no. 3, pp. 1640–1657, Jan. 2015.

[37] R. He, A. F. Molisch, F. Tufvesson, Z. Zhong, B. Ai, and T. Zhang, "Vehicle-to-vehicle propagation models with large vehicle obstructions," *IEEE Trans. Intell. Transp. Syst.*, vol. 15, no. 5, pp. 2237–2248, Oct. 2014.

[38] G. Y. Wang and Z. Bao, "The minimum entropy criterion of range alignment in ISAR motion compensation," *IEEE Radar Syst. (Radar)*, Edinburgh, U.K., Oct. 1997, pp. 236–239.

[39] M. Zhao, S. Zhu, B. Wu, and A. Zhang, "Simulations and measurement of 2D metamaterial aperture antenna," in *Proc. 6th Asia–Pacific Conf. Antennas Propag. (APCAP)*, Xi'an, China, Oct. 2017, pp. 1–3.

MENGRAN ZHAO (Graduate Student Member, IEEE) was born in Shijiazhuang, Hebei, China, in 1993. He received the B.S. degree in information engineering from Xi'an Jiaotong University, Xi'an, China, in 2016, where he is currently pursuing the Ph.D. degree in electronic science and technology. His research interests mainly include metasurface antenna with bunching random beams for coincidence imaging, mm-wave antenna design, and polarization-sensitive meta-material theory.

SHITAO ZHU received the B.S. degree in electronic information science and technology from Lanzhou University, Lanzhou, China, in 2005, and the M.S. degree in information and communication engineering, and the Ph.D. degree in electronic science and technology from Xi'an Jiaotong University, in 2008 and 2016, respectively. From 2008 to 2012, he was a System Engineer with ZTE Corporation, Ltd., Xi'an. He is currently an Associate Research Fellow with the School of Information and Communication Engineering, Xi'an Jiaotong University. He is also with the National Key Lab of Radar Signal Processing, Xidian University. His research interests include the metamaterial antenna, radar signal processing, and microwave coincidence imaging.

HUILIN HUANG received the B.S. degree in electronic information engineering from Xiamen University, Xiamen, China, in 2018. She is currently pursuing the M.S. degree in information engineering from Xi'an Jiaotong University. Her research interests include MIMO antennas and metasurface.

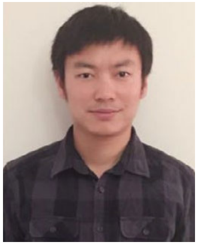

XIAOMING CHEN (Senior Member, IEEE) received the B.S. degree in electrical engineering from Northwestern Polytechnical University, Xi'an, China, in 2006, and the M.S. and Ph.D. degrees in electrical engineering from the Chalmers University of Technology, Gothenburg, Sweden, in 2007 and 2012, respectively. From 2013 to 2014, he was a Postdoctoral Researcher with the Chalmers University of Technology. From 2014 to 2017, he was with Qamcom Research & Technology AB, Gothenburg. Since 2017, he has been a Professor with Xi'an Jiaotong University, Xi'an, China. His research interests include MIMO antennas, over-the-air testing, reverberation chambers, and hardware impairments and mitigation.

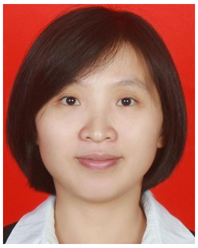

JUAN CHEN (Member, IEEE) received the Ph.D. degree in electro-magnetic and microwave engineering from Xi'an Jiaotong University, Xi'an, China, in 2008. From 2016 to 2017, she was a Visiting Researcher with the Department of Electrical and Computer Engineering, Duke University, Durham, NC, USA, under the financial support from the China Scholarship Council. She is currently a Professor with the Shenzhen Research School, Xi'an Jiaotong University, where she is also with the School of Electronic and Information Engineering. Her current research interests include numerical electro-magnetic methods, advanced antenna design, and grapheme theory and applications.

ANXUE ZHANG received the B.S. degree in electrical engineering from Henan Normal University, in 1996, and the M.S. and Ph.D. degrees in electromagnetic and microwave engineering from Xi'an Jiaotong University, in 1999 and 2003, respectively. He is currently a Professor with Xi'an Jiaotong University. His main research fields include metamaterials, RF and microwave circuit design, antenna and electromagnetic wave propagation.

• • •